Electron-phonon matrix elements in single-wall carbon nanotubes

doi: 10.1103/PhysRevB.72.235408

Electron-phonon matrix elements in single-wall carbon nanotubes

J. Jiang,[1] R. Saito,[1] Ge. G. Samsonidze,[2] S. G. Chou,[3] A. Jorio,[6] G. Dresselhaus,[5] and M. S. Dresselhaus[2,4]
[1]*Department of Physics, Tohoku University and CREST, JST, Sendai, 980-8578, Japan*
[2]*Department of Electrical Engineering and Computer Science, Massachusetts Institute of Technology, Cambridge, Massachusetts 02139, USA*
[3]*Department of Chemistry, Massachusetts Institute of Technology, Cambridge, Massachusetts 02139-4307, USA*
[4]*Department of Physics, Massachusetts Institute of Technology, Cambridge, Massachusetts 02139, USA*
[5]*Francis Bitter Magnet Laboratory, Massachusetts Institute of Technology, Cambridge, Massachusetts 02139, USA*
[6]*Departamento de Física, Universidade Federal de Minas Gerais, Belo Horizonte-MG, 30123-970 Brazil*
(Received 19 July 2005; revised manuscript received 11 October 2005; published 7 December 2005)

We have developed the electron-phonon matrix element in single-wall carbon nanotubes by using the extended tight-binding model based on density functional theory. We calculate this matrix element to study the electron-phonon coupling for the radial breathing mode (RBM) and the *G*-band *A* symmetry modes of single-wall carbon nanotubes. Three well-defined family patterns are found in the RBM, longitudinal optical (LO) mode and transverse optical (TO) mode. We find that among the RBM, LO, and TO modes, the LO mode has the largest electron-phonon interaction. To study the electron-phonon coupling in the transport properties of metallic nanotubes, we calculate the relaxation time and mean free path in armchair tubes. We find that the LO mode, A_1' mode, and one of the E_1' modes give rise to the dominant contributions to the electron inelastic backscattering by phonons. Especially, the off-site deformation potential gives zero matrix elements for E_1' modes while the on-site deformation potential gives rise to nonzero matrix elements for the two E_1' modes, indicating that the on-site deformation potential plays an important role in explaining the experimentally observed Raman mode around 2450 cm^{-1} in carbon.

DOI: 10.1103/PhysRevB.72.235408 PACS number(s): 78.67.−n, 78.40.−q, 78.30.−j

I. INTRODUCTION

The physical properties of a single-wall carbon nanotube (SWNT) are given by their cylindrical geometry denoted by (n,m).[1] Single-wall metallic carbon nanotubes are known to be conductors with mean free paths usually larger than one micron.[2,3] The use of semiconducting nanotubes as ballistic field effect transistors, provides innovative devices competitive in performance with silicon-based MOSFETs.[4,5]

Ballistic transport is restricted to low bias regimes, where the main origin of the resistivity is believed to be from inelastic scattering by acoustic phonons.[3,6–8] The scattering is weak, resulting in a long mean free path at room temperature. At high bias, the mobility is dramatically reduced by optical phonon emission, leading to interesting saturation behaviors.[9]

From the measured *I-V* curves, the scattering length is estimated to be $\ell \sim 10-18$ nm for optical phonon backscattering.[2,6] The theoretical ℓ_{op} varies within the range 10 to 200 nm.[2,6,10–12]

Transport experiments probe electron-phonon (el-ph) scattering near the Fermi level. Fast optics experiments, on the other hand, can probe the carrier lifetime far from the Fermi level.[13–15] Fast optics experiments on graphite found that the carrier lifetime is shorter than 1 ps,[14] which is consistent with theoretical calculations.[16] Curvature effects enhance the el-ph coupling and thus the experimentally observed intraband lifetime in SWNTs is shorter than 0.1 ps.[13,15]

Photoluminescence (PL) experiments[17] provide another tool to probe optically excited carrier relaxation processes in semiconducting nanotubes.[17–20] The PL intensity depends on the nanotube diameter and chiral angle.[17,20] Also, for type I $[\mathrm{mod}(2n+m,3)=1]$ and type II $[\mathrm{mod}(2n+m,3)=2]$ semiconducting tubes, the PL intensity shows a different diameter and chiral angle dependence,[20] which is argued to be caused by different phonon-assisted relaxation rates.[21,22]

Raman spectroscopy has provided an alternative method for studying vibrational properties of SWNTs.[23,24] The optical Γ and K point phonons are the phonons responsible for the Raman G and G' peaks in carbons, respectively.[24] The intensities of the Raman modes are determined by the el-ph matrix elements.[25,26] Recently, a very well pronounced qualitative effect has been observed in the Raman intensity from the radial breathing mode (RBM) of carbon nanotubes.[27,28] The RBM Raman intensity shows a well-defined dependence on tube type, diameter and chiral angle. This qualitative phenomenon has been explained by numerical studies.[26,28,29]

The el-ph interaction plays an important role in transport properties, fast optical spectroscopy, PL intensity, and Raman spectroscopy in SWNTs. So far, we have developed the el-ph interaction in SWNTs based on the tight-binding (TB) approximation.[16,18,26,30] Compared with simple TB, the extended TB (ETB) model[28,31,32] can describe well the curvature effect, especially for small diameter nanotubes.[31] The ETB model utilizes the TB transfer and overlap integrals as functions of the C-C interatomic distance calculated within a density-functional theory (DFT) framework.[33] The curvature effect is included by extending the basis set to the atomic s, p_x, p_y, and p_z orbitals that form the σ and π molecular orbitals.

The el-ph matrix elements for Γ point phonons can be obtained from the shift of the electronic energy bands under

deformation of the atomic structure corresponding to the phonon pattern.[34] Using the ETB,[32] Popov *et al.* calculated the el-ph matrix elements for the RBM by this method.[35,36] In this paper, we further develop the el-ph matrix elements based on the ETB, which includes curvature and long-range interactions. We use first-order perturbation theory, and the el-ph matrix element is assumed to be the potential variation due to a lattice vibration,[16,18,26,30] by which the el-ph coupling for a general **q** point phonon mode can be calculated. We then apply the method to calculate the RBM, LO, and TO mode matrix elements. Regular family patterns are found for these three modes.

We also calculate the matrix elements near the Fermi level of an armchair tube. We study the el-ph coupling for each mode in detail and find that among the 6Γ and $6K$ phonon modes, the LO, A_1', and E_1' modes dominate el-ph coupling. The el-ph interaction for LO and A_1' modes comes from the off-site deformation potential, while that for E_1' modes comes from the on-site deformation potential. The electron backscattering is mainly caused by the LO, A_1', and one of the E_1' modes. Because the on-site deformation potential gives rise to nonzero el-ph coupling for E_1' modes, it should be considered in order to explain the experimentally observed Raman peak around 2450 cm^{-1} in graphite.[37,38]

In Sec. II, we develop the el-ph matrix element expression based on the ETB. In Sec. III, we show the off-site and on-site deformation potential vectors. In Secs. IV and V, we study the family patterns in the el-ph matrix elements in the RBM and *G* band *A* symmetry modes, respectively. In Sec. VI, the relaxation time and mean free path in armchair tubes are calculated. Discussions and summary are given in Sec. VII.

II. ELECTRON-PHONON MATRIX ELEMENT BASED ON THE ETB

The Bloch wave function corresponding to the band index a and wave vector $\mathbf{k}$ can be written in the form

$$\Psi_{a,\mathbf{k}}(\mathbf{r}) = \frac{1}{\sqrt{N_u}} \sum_{s,o} C_{s,o}(a,\mathbf{k}) \sum_u e^{i\mathbf{k}\cdot\mathbf{R}_{u,s}} \phi_{s,o}(\mathbf{r}-\mathbf{R}_{u,s}), \quad (1)$$

where N_u is the number of graphite unit cells, $s=A$ and B, and $\mathbf{R}_{u,s}$ denotes the equilibrium atom position. $\phi_{s,o}$ are the atomic wave functions for the orbitals $o=2s$, $2p_x$, $2p_y$, and $2p_z$, respectively. The three orthogonal $2p$ orbitals $2p_x$, $2p_y$, and $2p_z$ for a carbon at site $\mathbf{R}_{u,s}$ are chosen to be tangential to the tube sidewall, along the tube axis, and along the radial direction, respectively. The atomic wave functions are selected as real functions. For SWNTs, $\mathbf{k}=\mu\mathbf{K}_1+k\mathbf{K}_2$ with $\mu=1,2,\ldots,N$ and $-\pi/T<k<\pi/T$. Here $\mathbf{K}_1$ and $\mathbf{K}_2$ are, respectively, the reciprocal lattice vectors along the circumferential and axial directions, T and N are, respectively, the 1D translational vector and the number of hexagons in the 1D nanotube unit cell.[1] Hereafter, we define $t\equiv(u,s)$ for convenience.

The Hamiltonian for a SWNT can be written as

$$H = -\frac{\hbar^2}{2m}\nabla^2 + V, \quad (2)$$

with

$$V = \sum_{\mathbf{R}_t} v(\mathbf{r}-\mathbf{R}_t), \quad (3)$$

where the first and second terms in Eq. (2) are, respectively, the kinetic and potential energies and v in Eq. (3) is the Kohn-Sham potential of a neutral pseudoatom.[33]

The matrix element for the potential energy between two states $\Psi_i=\Psi_{a,\mathbf{k}}$ and $\Psi_f=\Psi_{a',\mathbf{k}'}$ is

$$\langle\Psi_{a',\mathbf{k}'}(\mathbf{r})|V|\Psi_{a,\mathbf{k}}(\mathbf{r})\rangle = \frac{1}{N_u}\sum_{s',o'}\sum_{s,o} C^*_{s',o'}(a',\mathbf{k}')C_{s,o}(a,\mathbf{k}) \times \sum_{u'}\sum_{u} e^{i(-\mathbf{k}'\cdot\mathbf{R}_{u',s'}+\mathbf{k}\cdot\mathbf{R}_{u,s})} m(t',o',t,o), \quad (4)$$

with the atomic matrix element given by

$$m = \int \phi_{s',o'}(\mathbf{r}-\mathbf{R}_{t'})\left(\sum_{\mathbf{R}_{t''}} v(\mathbf{r}-\mathbf{R}_{t''})\right)\phi_{s,o}(\mathbf{r}-\mathbf{R}_t)d\mathbf{r}. \quad (5)$$

As usual, one can neglect several contributions to the atomic matrix element m.[33] By keeping only two-center atomic matrix elements ($\mathbf{R}_{t''}=\mathbf{R}_{t'}$, or $\mathbf{R}_{t''}=\mathbf{R}_t$, or $\mathbf{R}_t=\mathbf{R}_{t'}$), Eq. (5) becomes

$$m = m_\alpha + m_\lambda, \quad (6)$$

with off-site and on-site matrix elements m_α and m_λ,

$$m_\alpha = \int \phi_{s',o'}(\mathbf{r}-\mathbf{R}_{t'})\{v(\mathbf{r}-\mathbf{R}_{t'})+v(\mathbf{r}-\mathbf{R}_t)\} \times \phi_{s,o}(\mathbf{r}-\mathbf{R}_t)d\mathbf{r},$$

$$m_\lambda = \delta_{\mathbf{R}_t,\mathbf{R}_{t'}}\int \phi_{s',o'}(\mathbf{r}-\mathbf{R}_{t'})\left(\sum_{\mathbf{R}_{t''}\neq\mathbf{R}_{t'}} v(\mathbf{r}-\mathbf{R}_{t''})\right) \times \phi_{s',o}(\mathbf{r}-\mathbf{R}_{t'})d\mathbf{r}. \quad (7)$$

A periodic displacement of atoms around the equilibrium sites gives rise to the el-ph interaction. The potential variation due to a lattice vibration is given by

$$\delta V = \sum_{\mathbf{R}_t} v[\mathbf{r}-\mathbf{R}_t-\mathbf{S}(\mathbf{R}_t)] - v(\mathbf{r}-\mathbf{R}_t) \approx -\sum_{\mathbf{R}_t}\nabla v(\mathbf{r}-\mathbf{R}_t)\cdot\mathbf{S}(\mathbf{R}_t), \quad (8)$$

where $\mathbf{S}(\mathbf{R}_t)$ is the site position deviation from the equilibrium site $\mathbf{R}_t$ caused by a vibration. Under first-order perturbation theory, the el-ph matrix element is defined as[16,18,26,30]

$$M_{a,\mathbf{k}\to a',\mathbf{k}'} = \langle \Psi_{a',\mathbf{k}'}(\mathbf{r})|\delta V|\Psi_{a,\mathbf{k}}(\mathbf{r})\rangle = -\frac{1}{N_u}\sum_{s',o'}\sum_{s,o} C^*_{s',o'}(a',\mathbf{k}')C_{s,o}(a,\mathbf{k}) \times \sum_{u',u} e^{i(-\mathbf{k}'\cdot\mathbf{R}_{u',s'}+\mathbf{k}\cdot\mathbf{R}_{u,s})}\delta m(t',o',t,o), \quad (9)$$

where $\delta m(t',o',t,o)$ is the atomic deformation potential. Similar to Eq. (6), δm can also be separated into two parts,

$$\delta m = \delta m_\alpha + \delta m_\lambda, \quad (10)$$

with the off-site and on-site deformation potential δm_α and δm_λ given, respectively, by

$$\delta m_\alpha = \int \phi_{s',o'}(\mathbf{r}-\mathbf{R}_{t'})\{\nabla v(\mathbf{r}-\mathbf{R}_{t'})\cdot\mathbf{S}(\mathbf{R}_{t'}) + \nabla v(\mathbf{r}-\mathbf{R}_t)\cdot\mathbf{S}(\mathbf{R}_t)\}\phi_{s,o}(\mathbf{r}-\mathbf{R}_t)d\mathbf{r},$$

$$\delta m_\lambda = \delta_{\mathbf{R}_t,\mathbf{R}_{t'}}\int \phi_{s',o'}(\mathbf{r}-\mathbf{R}_{t'}) \times \left(\sum_{\mathbf{R}_{t''}\neq\mathbf{R}_{t'}} \nabla v(\mathbf{r}-\mathbf{R}_{t''})\cdot\mathbf{S}(\mathbf{R}_{t''})\right)\phi_{s',o}(\mathbf{r}-\mathbf{R}_{t'})d\mathbf{r}. \quad (11)$$

In the Slater-Koster scheme to construct the tight-binding Hamiltonian matrix elements between two carbon atoms,[33] the carbon $2p$ orbitals are chosen to be along or perpendicular to the bond connecting the two atoms. The four fundamental hopping and overlap integrals are (ss), $(s\sigma)$, $(\sigma\sigma)$, and $(\pi\pi)$. We follow the same way to construct the deformation potential matrix elements $\langle\phi|\nabla v|\phi\rangle$. We introduce the matrix elements,

$$\vec{\alpha}_p(\tau) = \int \phi_\mu(\mathbf{r})\,\nabla\, v(\mathbf{r})\phi_\nu(\mathbf{r}-\tau)d\mathbf{r} = \alpha_p(\tau)\hat{I}(\alpha_p),$$

$$\vec{\lambda}_p(\tau) = \int \phi_\mu(\mathbf{r})\,\nabla\, v(\mathbf{r}-\tau)\phi_\nu(\mathbf{r})d\mathbf{r} = \lambda_p(\tau)\hat{I}(\lambda_p), \quad (12)$$

where $\hat{I}(\alpha_p)$ and $\hat{I}(\lambda_p)$ are unit vectors describing the direction of the off-site and on-site deformation potential vectors $\vec{\alpha}_p$ and $\vec{\lambda}_p$, respectively,[39] and $p=\mu\nu$. The $2p$ orbital $\phi_\mu(\phi_\nu)$ is along or perpendicular to the bond connecting the two atoms and τ is the distance between the two atoms. From the matrix element $\vec{\alpha}_p$, we can deduce another matrix element,

$$\vec{\beta}_p(\tau) = \int \phi_\mu(\mathbf{r})\,\nabla\, v(\mathbf{r}-\tau)\phi_\nu(\mathbf{r}-\tau)d\mathbf{r} = \int \phi_\nu(\mathbf{r})\,\nabla\, v(\mathbf{r})\phi_\mu(\mathbf{r}+\tau)d\mathbf{r} = \beta_p(\tau)\hat{I}(\beta_p). \quad (13)$$

By projecting the $2p_x$, $2p_y$, and $2p_z$ orbitals on $\mathbf{R}_t$ and $\mathbf{R}_{t'}$ sites along or perpendicular to the direction connecting these two sites and using the matrix elements defined in Eqs. (12) and (13), the atomic deformation potential in Eq. (11) can be written as

$$\delta m_\alpha = \left(\sum_p \chi^p_{o'o}\vec{\alpha}_p(|\mathbf{R}_t-\mathbf{R}_{t'}|)\right)\cdot\mathbf{S}(\mathbf{R}_{t'}) + \left(\sum_p \chi^p_{o'o}\vec{\beta}_p(|\mathbf{R}_t-\mathbf{R}_{t'}|)\right)\cdot\mathbf{S}(\mathbf{R}_t),$$

$$\delta m_\lambda = \delta_{\mathbf{R}_t,\mathbf{R}_{t'}}\sum_{\mathbf{R}_{t''}\neq\mathbf{R}_{t'}}\left(\sum_p \chi^p_{o'o}\vec{\lambda}_p(|\mathbf{R}_{t''}-\mathbf{R}_{t'}|)\right)\cdot\mathbf{S}(\mathbf{R}_{t''}), \quad (14)$$

where $\chi^p_{o'o}$ is the coefficient to project the orbitals o' and o onto the orbitals used in the Slater-Koster scheme to construct the deformation potential matrix elements Eqs. (12) and (13). The vibration $\mathbf{S}(\mathbf{R}_t)$ for the phonon mode $(\nu,\mathbf{q})$ is

$$\mathbf{S}(\mathbf{R}_t) = A_\nu(\mathbf{q})\sqrt{\bar{n}_\nu(\mathbf{q})}\mathbf{e}^\nu(\mathbf{R}_t)e^{\pm i\omega_\nu(\mathbf{q})t}. \quad (15)$$

Here $\pm$ is for phonon emission $(+)$ and absorption $(-)$, respectively, and A, $\bar{n}$, $\mathbf{e}$, and ω are the phonon amplitude, number, eigenvector, and frequency, respectively.

At equilibrium, the phonon number in Eq. (15) is determined by the Bose-Einstein distribution function n,

$$n_\nu(\mathbf{q}) = \frac{1}{e^{\hbar\omega/k_BT}-1}. \quad (16)$$

Here T is the lattice temperature and k_B is the Boltzmann constant. For phonon emission, the phonon number is $\bar{n}=n+1$ and for phonon absorption, it is $\bar{n}=n$.

The amplitude of the phonon vibration is

$$A_\nu(\mathbf{q}) = \sqrt{\frac{\hbar}{N_u m_C\omega_\nu(\mathbf{q})}}, \quad (17)$$

and the phonon eigenvector $\mathbf{e}^\nu(\mathbf{R}_t)$ is given by

$$\mathbf{e}^\nu(\mathbf{R}_{u,s}) = e^{i\mathbf{q}\cdot\mathbf{R}_{u,s}}U(\phi)\mathbf{e}^\nu_\mathbf{q}(s). \quad (18)$$

Here U is the rotation from an s atom in a graphite unit cell to an atom at a $\mathbf{R}_{u,s}$ site, and $\mathbf{e}^\nu_\mathbf{q}(s)$ is the phonon eigenvector calculated by diagonalizing the N 6×6 dynamical matrices for a SWNT.[1,18]

In Eq. (9) we have not written out the phase factor $e^{i[\epsilon(a',\mathbf{k}')-\epsilon(a,\mathbf{k})]t}$ with $\epsilon(a,\mathbf{k})$ and $\epsilon(a',\mathbf{k}')$ the initial and final state energies. This phase factor when combined with the phase factor for phonon vibration in Eq. (15) gives energy conservation in an electron-phonon scattering process.

Substituting Eq. (15) into Eq. (14), the el-ph matrix element from the $(a,\mathbf{k})$ to $(a',\mathbf{k}')$ electronic state coupled by the νth phonon is given by,

$$M^\nu_{a,\mathbf{k}\to a',\mathbf{k}'} = -\frac{1}{\sqrt{N_u}}\sqrt{\bar{n}_\nu(\mathbf{q})}g^\nu_{a,\mathbf{k}\to a',\mathbf{k}'}. \quad (19)$$

Here

$$g^\nu_{a,\mathbf{k}\to a',\mathbf{k}'} = \left(\frac{\hbar}{m_C\omega_\nu(\mathbf{q})}\right)^{1/2}D^\nu_{a,\mathbf{k}\to a',\mathbf{k}'}, \quad (20)$$

with the matrix element D given by

$$D^{\nu}_{o\to o'}(a,\mathbf{k}\to a',\mathbf{k}') = \sum_{s'} C^{*}_{s',o'}(a',\mathbf{k}')C_{s',o}(a,\mathbf{k})\sum_{u,s}\left(\sum_{p}\chi^{p}_{o'o}\vec{\lambda}_{p}(|\mathbf{R}_{u,s}-\mathbf{r}_{s'}|)\right)\cdot\mathbf{e}^{\nu}_{\mathbf{k}'-\mathbf{k}}(\mathbf{R}_{u,s})e^{-i(\mathbf{k}'-\mathbf{k})\cdot\mathbf{r}_{s'}}$$
$$+\sum_{s',s} C^{*}_{s',o'}(a',\mathbf{k}')C_{s,o}(a,\mathbf{k})\sum_{u} e^{i\mathbf{k}\cdot(\mathbf{R}_{u,s}-\mathbf{r}_{s'})}e^{-i(\mathbf{k}'-\mathbf{k})\cdot\mathbf{r}_{s'}}\left[\left(\sum_{p}\chi^{p}_{o'o}\vec{\alpha}_{p}(|\mathbf{R}_{u,s}-\mathbf{r}_{s'}|)\right)\cdot\mathbf{e}^{\nu}_{\mathbf{k}'-\mathbf{k}}(\mathbf{r}_{s'})\right.$$
$$\left.+\left(\sum_{p}\chi^{p}_{o'o}\vec{\beta}_{p}(|\mathbf{R}_{u,s}-\mathbf{r}_{s'}|)\right)\cdot\mathbf{e}^{\nu}_{\mathbf{k}'-\mathbf{k}}(\mathbf{R}_{u,s})\right], \tag{21}$$

and

$$D^{\nu}_{a,\mathbf{k}\to a',\mathbf{k}'} = \sum_{o',o} D^{\nu}_{o\to o'}(a,\mathbf{k}\to a',\mathbf{k}'), \tag{22}$$

where $\mathbf{r}_{s'}=\mathbf{R}_{0,s'}$ is the equilibrium position for atom s' in a graphite unit cell and $\mathbf{R}_{u,s}\neq\mathbf{r}_{s'}$. In the derivation of Eq. (21), the summation over u',

$$\frac{1}{N_u}\sum_{u'} e^{i(\mathbf{k}-\mathbf{k}'+\mathbf{q})\cdot(\mathbf{R}_{u',s'}-\mathbf{r}_{s'})}, \tag{23}$$

gives momentum conservation $\mathbf{q}=\mathbf{k}'-\mathbf{k}$.

The matrix elements are given by an inner product of the atomic deformation potential vectors ($\vec{\alpha}$, $\vec{\beta}$, and $\vec{\gamma}$) and the phonon eigenvectors. An important thing to note is that we need to take a summation over $\mathbf{R}_{u,s}$, which is a neighbor site of an *A* or *B* atom in the graphite unit cell. From the followed Sec. III, we will see that the atomic deformation potential [$\alpha(r)$, $\beta(r)$, and $\gamma(r)$] can extend to several Å. Thus, in the calculation, we need to consider up to several nearest neighbors.

III. DEFORMATION POTENTIAL VECTORS

There are nine nonzero deformation potential vectors $\vec{\alpha}_p$, which are shown in Fig. 1. Among them, the vectors in Figs. 1(1)–(5) are along the bond connecting the two orbitals. The other four vectors in Fig. 1(6)–(9) are the deformation potential matrix elements with a π orbital and have a direction along the π orbital.

The corresponding nonzero potential vectors $\vec{\beta}_p$ are shown in Fig. 2. From Fig. 1 and Fig. 2, it is easy to find the following relationships between $\vec{\beta}_p$ and $\vec{\alpha}_p$:

$$\vec{\beta}_{ss}=-\vec{\alpha}_{ss},\quad \vec{\beta}_{s\sigma}=\vec{\alpha}_{\sigma s},$$
$$\vec{\beta}_{\sigma s}=\vec{\alpha}_{s\sigma},\quad \vec{\beta}_{\sigma\sigma}=-\vec{\alpha}_{\sigma\sigma},$$
$$\vec{\beta}_{\pi\pi}=-\vec{\alpha}_{\pi\pi},\quad \vec{\beta}_{s\pi}=\vec{\alpha}_{\pi s},$$
$$\vec{\beta}_{\pi s}=\vec{\alpha}_{s\pi},\quad \vec{\beta}_{\sigma\pi}=-\vec{\alpha}_{\pi\sigma},$$
$$\vec{\beta}_{\pi\sigma}=-\vec{\alpha}_{\sigma\pi}. \tag{24}$$

For on-site deformation potential vectors $\vec{\lambda}_p$, there are six nonzero matrix elements, which are shown in Fig. 3. The four vectors in Fig. 3(1)–(4) are along the bond direction while the two vectors in Fig. 3(5)–(6) are perpendicular to the bond and along the π orbital direction.

The RBM vibration is perpendicular to the nanotube sidewall. Thus, the el-ph matrix element $D_{o\to o'}$ of the RBM by the potential vectors in Fig. 1(6)–(9) and Fig. 3(5)–(6), which are perpendicular to the bond, should be large.

The values of the matrix elements α_p and λ_p depend only on interatomic distances. To make a self-consistent calculation of the deformation potential matrix elements, we use the same atomic wave functions and Kohn-Sham potential as those used in Ref. 33, which are calculated by density functional theory.[33] In Figs. 4 and 5, we show the matrix elements α_p and λ_p versus the two carbon-carbon interatomic separation. Figures 4(a) and 5(a) are the matrix elements with the corresponding vectors along the bond direction. Fig-

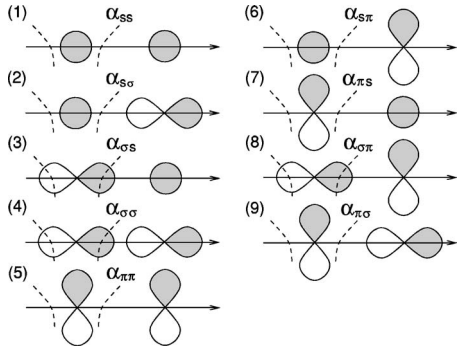

FIG. 1. The nine nonzero off-site deformation potential vectors $\vec{\alpha}_p$. The dashed curves represent the atomic potential.

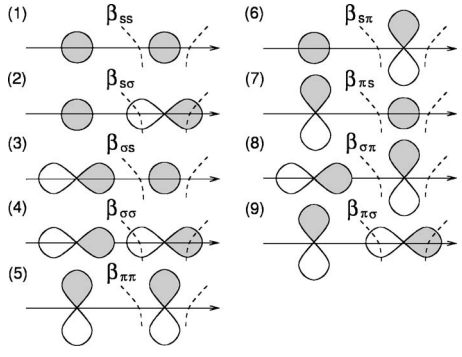

FIG. 2. The nine nonzero off-site deformation potential vectors. $\vec{\beta}_p$. The dashed curves represent the atomic potential.

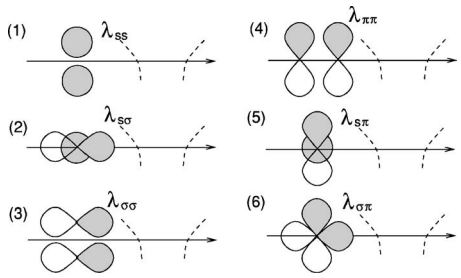

FIG. 3. The six nonzero on-site deformation potential vectors $\vec{\beta}_p$. The dashed curves represent the atomic potential. For λ_{ss}, $\lambda_{\sigma\sigma}$, $\lambda_{\pi\pi}$ two same orbitals are illustrated by shifting them with respect to each other.

ures 4(b) and 5(b) show the matrix elements with the corresponding vectors perpendicular to the bond direction. At $r=1.42$ Å, the bond length between a carbon and one of its nearest neighbors, $\alpha_{\pi\pi}\approx 3.2$ eV/Å and $|\lambda_{\pi\pi}|\approx 7.8$ eV/Å. The present $\alpha_{\pi\pi}$ has a very similar value as that calculated by using the π orbital wave function and the atomic potential of a free carbon.[16,18] However, the present $|\lambda_{\pi\pi}|$ value has been enhanced by about 1.1 eV/Å from that by previous methods.[16,18] It follows that in the framework of the ETB the on-site deformation potential will play a more important role in the el-ph coupling.

At $r=1.42$ Å, $|\alpha_{\pi\sigma}|$ in Fig. 4(b) is about 24.9 eV/Å, which is approximately 7.8 times larger than $\alpha_{\pi\pi}$ in Fig. 4(a). Thus, the σ orbital will give a significant contribution to the matrix element $D_{o\to o'}$ of the RBM.

IV. FAMILY PATTERNS OF ELECTRON-PHONON MATRIX ELEMENTS IN THE RBM

We use the ETB model to calculate the electron wave functions, when the curvature effect, long-rang interactions

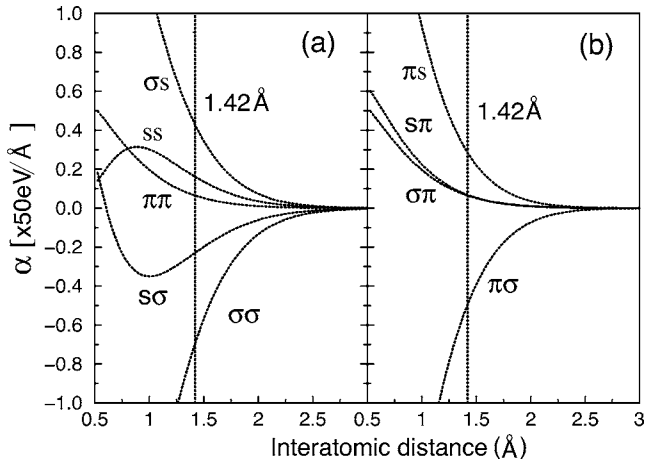

FIG. 4. The dependence of the nine off-site deformation potential matrix elements α_p on interatomic distance. (a) The matrix elements with the corresponding deformation potential vectors $\vec{\alpha}_p$ along the bond of the two atoms. (b) The matrix elements with the corresponding deformation potential vectors $\vec{\alpha}_p$ perpendicular to the bond of the two atoms. The nearest-neighbor distance between two carbon atoms is $a_{c-c}=1.42$ Å.

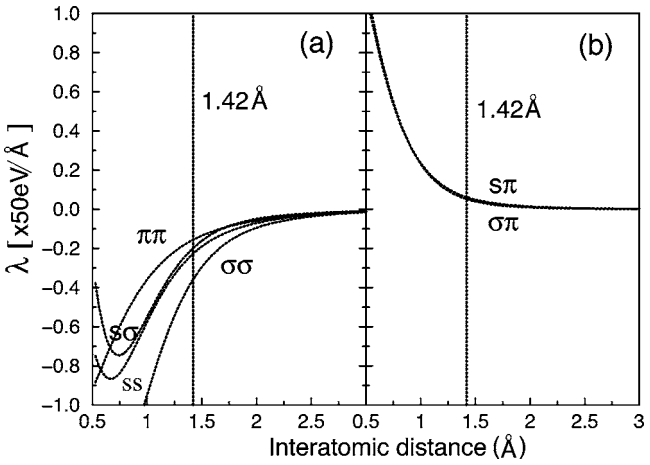

FIG. 5. The six on-site deformation potential matrix elements λ_p as a function of interatomic distance. (a) The matrix elements with the corresponding deformation potential vectors $\vec{\lambda}_p$ along the bond of the two atoms. (b) The matrix elements with the corresponding deformation potential vectors $\vec{\lambda}_p$ perpendicular to the bond of the two atoms. The nearest-neighbor distance between two carbon atoms is $a_{c-c}=1.42$ Å

of σ and π orbitals and the geometrical structure optimization are all considered.[31] We further use the carbon orbital basis functions and the carbon Kohn-Sham potential by DFT[33] to construct the deformation potential matrix elements. It is known that the ETB can well describe the family behavior of the optical transition energy in SWNTs of small diameter.[31] Here by using the el-ph matrix elements in the ETB framework, we calculate the el-ph coupling for the RBM and G band phonon modes. We find that regular family patterns also exist in the matrix elements for the RBM, LO, and TO modes.

For phonon modes appearing in first order Raman processes, $\mathbf{q}=0$, the el-ph matrix element g defined in Eq. (20) can be expressed as $g=g_{c,\mathbf{k}\to c,\mathbf{k}}-g_{v,\mathbf{k}\to v,\mathbf{k}}$ with $g_{c,\mathbf{k}\to c,\mathbf{k}}$ and $g_{v,\mathbf{k}\to v,\mathbf{k}}$ the matrix elements for the conduction and valence π bands, respectively. We calculate the matrix elements for the E_{ii} transitions for nanotubes with diameters in the range of 0.6 nm$<d_t<$2.0 nm. Figures 6 and 7 show the matrix element for the RBM for semiconducting tubes at E_{22}^S transitions. Here we show $|g|$, the magnitude of the matrix element. We classify semiconducting nanotubes into two kinds, i.e., the mod$(2n+m,3)=1$ type I (SI) and mod$(2n+m,3)=2$ type II (SII) semiconducting nanotubes.[28,31,40] Within a specific type, we connect SWNTs with the same $(n-m)$ value (same family). Figures 6(a) and 7(a) are for SI tubes while Figs. 6(b) and 7(b) are for SII tubes. Regular family patterns are seen in both the $|g|$ vs inverse of diameter (d_t) and $|g|$ vs chiral angle (θ) figures. Figures 8 and 9 show the matrix elements for metallic tubes at E_{11}^M transitions. For metallic nanotubes, the trigonal warping effect in the energy dispersion relation splits each van Hove singularity (vHS) E_{ii}^M peak in the joint density of states into two peaks (E_{iiL}^M and E_{iiH}^M, denoting the lower and higher energy peaks).[41] Figures 8(a) and 9(a) are for E_{iiL}^M transitions and Figs. 8(b) and 9(b) are for E_{iiH}^M transitions. The family patterns are also observed in Figs. 8 and 9.

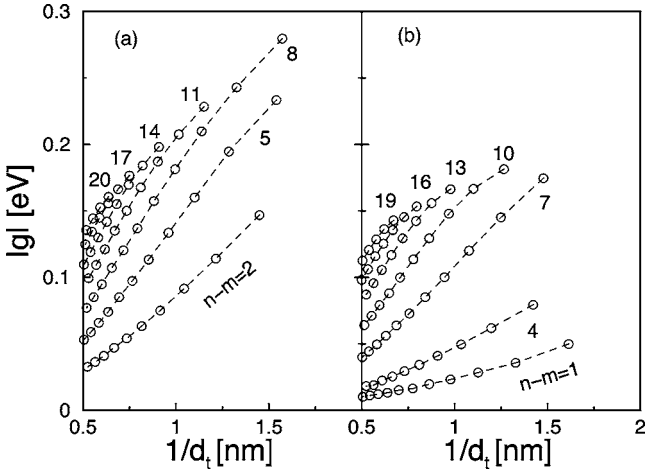

FIG. 6. Family patterns in the el-ph matrix element vs inverse of diameter at E_{22}^S transitions for the RBM, (a) SI and (b) SII tubes. The family numbers for $n-m$ are shown in the figures.

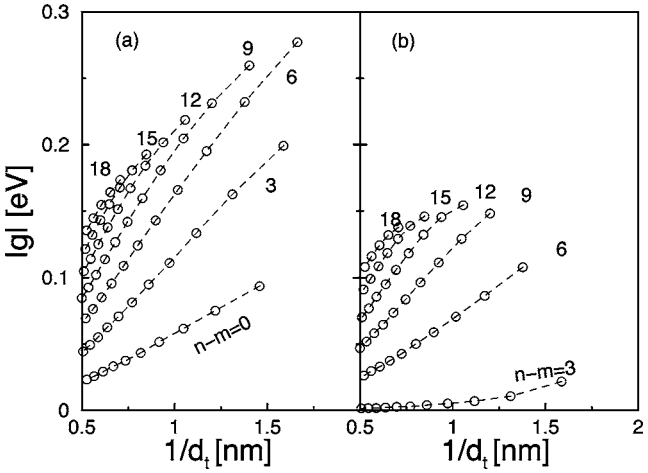

FIG. 8. Family patterns in the el-ph matrix element vs inverse of diameter at E_{11}^M transitions for the RBM of metallic tubes, (a) E_{11L}^M and (b) E_{11H}^M. The family numbers for $n-m$ are shown in the figures.

We should mention that in the present approximation, the contribution from $\alpha_{\pi\sigma}$ to $g_{p_x\to p_z}$ ($g_{p_z\to p_x}$) and $g_{p_y\to p_z}$ ($g_{p_z\to p_y}$) is found to be overestimated, by comparing the contribution from $\alpha_{\pi\sigma}$ to $g_{p_z\to p_z}$. To get comparable values to those obtained by *ab initio* method for several nanotubes,[29] in the calculations of the data shown in Figs. 6–9, this contribution has been multipled by a factor 0.8.

V. FAMILY PATTERNS OF ELECTRON-PHONON MATRIX ELEMENTS IN *G* BAND *A* SYMMETRY MODES

The matrix elements $|g|$ for the LO mode for semiconducting tubes at E_{22}^S transitions are shown in Fig. 10, which shows different family patterns than the RBM. For the RBM, $|g|$ decreases with d_t for both SI and SII tubes. For the LO mode $|g|$ decreases and increases with d_t for SI and SII tubes. Also, $|g|$ decreases and increases with θ for SI and SII tubes. We note that the values of $|g|$ in Fig. 10 are distributed in a narrow range around a nonzero value, while $|g|$ in the RBM are distributed from zero (or close to zero) to a nonzero value, indicating that the matrix element for the LO mode has less d_t and θ dependence than that for the RBM mode. The reason is that the matrix element for the LO mode is related to that for the G band of graphite in the limit of $1/d_t=0$. For the LO mode, g has an opposite sign for vHSs on the two sides of the BZ.[26] Figure 10(b) shows that $|g|$ tends to be the same for two vHSs on the two different side of the BZ around a K point. For an armchair tube, there are two vHSs on the two sides of the BZ for a E_{ii} transition. The el-ph matrix elements for these two vHSs have opposite values. It follows that the Raman intensity contributions from these two vHSs cancel each other perfectly and the Raman intensity for the LO mode becomes zero.

Figures 11 and 12 show the matrix element $|g|$ for the TO mode for the E_{22}^S transition. For the RBM and LO modes, g has an opposite sign for vHSs on the two sides of the BZ (Ref. 26) and thus we show $|g|$ rather than g. For the TO

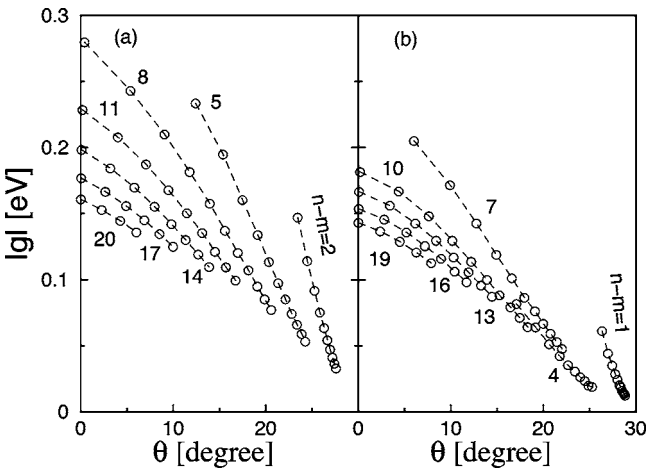

FIG. 7. Family patterns in the el-ph matrix element vs chiral angle at E_{22}^S transitions for the RBM, (a) SI and (b) SII tubes. The family numbers for $n-m$ are shown in the figures.

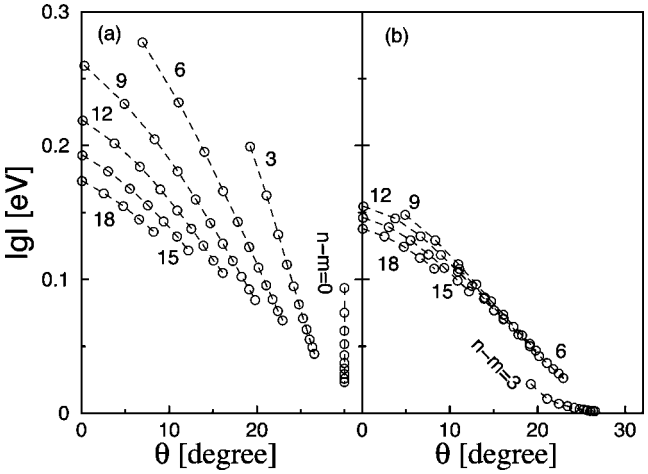

FIG. 9. Family patterns in the el-ph matrix element vs chiral angle at E_{11}^M transitions for the RBM of metallic tubes, (a) E_{11L}^M and (b) E_{11H}^M. The family numbers for $n-m$ are shown in the figures.

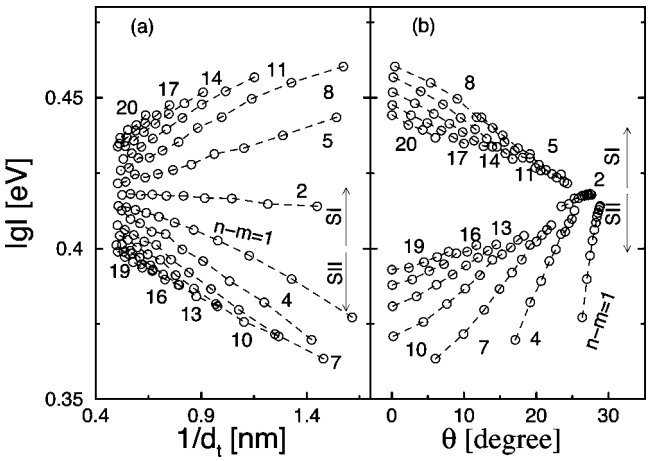

FIG. 10. The family patterns in the el-ph matrix element at E_{22}^S transitions for the LO mode, (a) the matrix element vs inverse of diameter and (b) the matrix element vs chiral angle. The family numbers for $n-m$ are shown in the figures.

mode, g has the same sign for vHSs on the two sides of the BZ.[26] Thus in Figs. 11 and 12 we show g. Unlike the RBM and LO modes, where the matrix elements show different family patterns for SI and SII tubes, g for the TO mode has very similar family patterns for SI and SII tubes.

In the first order Raman excitation profiles, both the peak intensity and linewidth are proportional to $|g|^2$. The family patterns in the el-ph matrix elements thus bring similar family patterns in the Raman intensity and linewidth. By considering that the measured Raman intensity is also dependent on the (n,m) sample population, the family patterns in the Raman intensity can be used to characterize the sample population. By measuring the fully resonant Raman intensity for each specific nanotube in the sample, and correcting for the calculated (n,m) dependent Raman cross section,[26] the amount of each specie in the sample is obtained.[42] The linewidth does not depend on the sample population but is sensitive to the environment. However, for suspended nanotubes in the ideal case, the linewidth should become intrinsic.

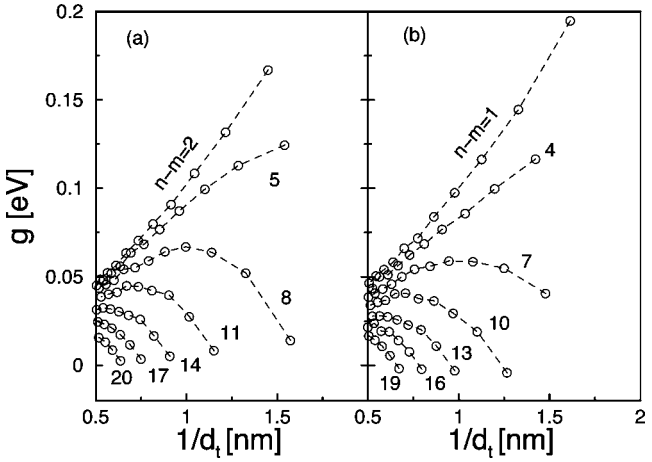

FIG. 11. The family patterns in the el-ph matrix element vs inverse of diameter at E_{22}^S transitions for the TO mode, (a) SI and (b) SII tubes. The family numbers for $n-m$ are shown in the figures.

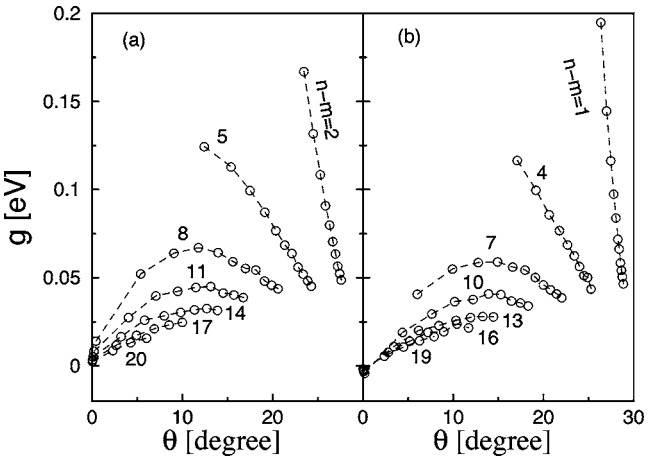

FIG. 12. The family patterns in the el-ph matrix element vs chiral angle at E_{22}^S transitions for the TO mode, (a) SI and (b) SII tubes. The family numbers for $n-m$ are shown in the figures.

Therefore, the family patterns in the linewidth of the suspended nanotubes can directly be used to characterize (n,m) species.

From Figs. 6–12, it is seen that the matrix elements for the LO mode are generally larger than those for the RBM and TO modes. The result that the LO mode has larger matrix elements than the RBM and TO modes can explain the experimental observations that generally the Raman intensity for the LO mode is larger than that for the RBM and TO modes. For suspended tube samples, the Raman intensity of the RBM can exceed that of the LO mode. The reasons are as follows. For a usual SWNT sample, e.g., a sodium dodecyl sulfate wrapped SWNT sample, the intensity linewidth has similar values for the RBM and LO modes due to an environmental effect. The LO mode has a larger el-ph matrix element and thus a larger Raman intensity. For a suspended sample, the linewidth should become intrinsic and is proportional to $|g|^2$. The RBM has a smaller $|g|$ value and thus a smaller linewidth. Therefore, even though the RBM has a smaller el-ph matrix element, it can have a larger intensity due to its smaller linewidth.

We note that the d_t and θ dependences of the el-ph matrix element shown in Figs. 6–12 are generally consistent with those obtained by the simple TB model.[26] However, the detailed family patterns by these two methods are different to some extent. Moreover, it is worth to point out that in Fig. 7, g for family $n-m=1$ has an opposite sign than g for other families, indicating the existence of a node around the tubes with family numbers 1 and 4, which is consistent with the prediction by the simple TB model. The existence of a node in SII tubes at the E_{22}^S transition has been confirmed by experiment.[43]

VI. RELAXATION TIME AND MEAN FREE PATH IN ARMCHAIR TUBES

Equation (21) indicates that the el-ph matrix element is sensitive to the phonon eigenvector. In the literature there are several sets of phonon dispersion theories for graphite and

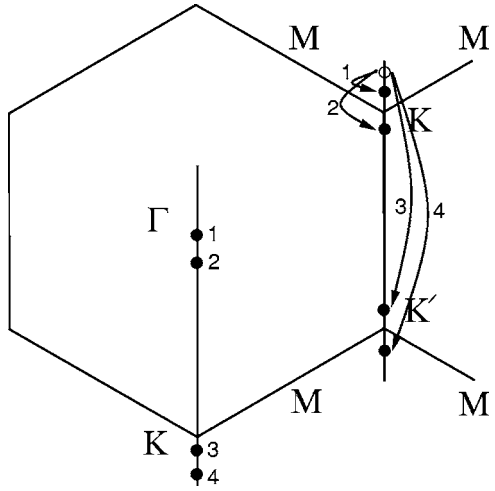

FIG. 13. The electron-phonon scattering processes near the Fermi level (the K and K' points) of an armchair tube. The processes 1 and 2 are the intravalley forward and backward scattering, respectively, and the corresponding phonons are around the Γ point. The processes 3 and 4 are the intervalley forward and backward scattering, respectively, and the corresponding phonons are around the K point.

the phonon dispersion obtained from these theories are different from one another.[44] The phonon theories for SWNTs, which are generally based on the phonon theory for graphite by including the curvature effect, are thus also different from each other. As a result, for a general **q** point in the 2D BZ of graphite, the phonon eigenvectors obtained by these theories are different from each other. For high symmetry **q** points, the phonon eigenvectors are determined only by symmetry, which is independent of which phonon dispersion theory is used. Therefore, for these high symmetry **q** points, we can study the el-ph interaction, which is independent of the phonon dispersion theory that is used.

The optical phonons at the Γ and K points are the phonons responsible for the Raman G and G' peaks in carbon. In graphite, there are six Γ phonons, i.e., the out-of-plane transverse acoustic (oTA), longitudinal acoustic (LA), in-plane transverse acoustic (iTA), out-of-plane transverse optical (oTO), in-plane TO (iTO), and longitudinal optical (LO) modes listed in order of increasing phonon frequency.[1] There are also $6K$ point phonons, i.e., a twofold degenerate E_2', a A_2', a twofold degenerate E_1', and a A_1' mode, again listed in order of increasing phonon frequency.[45]

When we turn to SWNTs, the cutting line[46] for metallic bands of an armchair tube passes through the edge KK' of the 2D BZ shown in Fig. 13. Near the Fermi level there are four kinds of electron-phonon scattering processes. The phonon modes for intravalley forward and backward scattering (processes 1 and 2 in Fig. 13) are those around the Γ point modes. The phonon modes for intervalley forward and backward scattering (processes 3 and 4 in Fig. 13) are those around the K point modes. Therefore, for electron-phonon scattering near the Fermi level, we have six Γ point modes, i.e., LA, twisting (TW), RBM, oTO, TO, and LO, and six K point modes, i.e., $2E_2'$, A_2', $2E_1'$, and A_1'. For armchair tubes the two degenerate E' modes are split in frequency due to the curvature effect. Here we still use E' to label these two modes for convenience. These 12 phonon modes are around the Γ or K point and are on the high symmetry line ΓK. It follows that the eigenvectors for these modes are not sensitive to the phonon dispersion theories. Moreover, the el-ph coupling near the Fermi level is not sensitive to the initial state since the electrons near the Fermi level have approximately the same wave functions.

In Table I we list the el-ph coupling strength ($|D|$), relaxation time (τ) and mean free path (ℓ) of a (10,10) tube for each mode for electrons with an initial state energy 0.25 eV above the Fermi level. The phonon frequencies for the modes near the Γ and K points are also listed. From Eq. (20), we know that g and D are the matrix elements normalized and

TABLE I. The el-ph coupling strength $|D|$, relaxation time τ, and mean free path ℓ for each mode near the Fermi level of a (10,10) tube. The wavevector q used to express $|D|$ for the TW mode is in units of Å^{-1}

		Forward			Backward		
Mode	Freq. (cm^{-1})	$\|D\|$ (eV/Å)	τ (ps)	ℓ (nm)	$\|D\|$ (eV/Å)	τ (ps)	ℓ (nm)
LA	0	0	0		0	0	
TW	0	0	0		$2.462q$	2.14	1812.2
RBM	187.10	1.53	0.56	469.9	0	0	
oTO	889.85	0	0		9.94	1.25	8354.1
iTO	1591.51	7.17	0.56	470.1	0	0	
LO	1595.51	0	0		6.66	0.65	546.8
$E_2'(1)$	527.69	1.91	1.57	1320.0	0	0	
$E_2'(2)$	545.47	0	0		0.95	8.72	7326.6
A_2'	988.82	0.48	39.6	33267.3	0	0	
$E_1'(1)$	1231.76	11.22	0.18	154.6	0	0	
$E_1'(2)$	1249.52	0	0		10.82	0.20	165.6
A_1'	1368.88	0	0		9.94	0.27	228.2

not normalized with the phonon energy, respectivelty. To show the el-ph coupling strength that is independent on the phonon dispersion, in this section we show the magnitude of the matrix element $|D|$ rather than $|g|$. For a given energy, there are two initial states around a K point with one on the line ΓK and the other on the line KM. The el-ph matrix elements around a K point are sensitive to the electron wavevector. The matrix element on the ΓK line may have a quite different value than that on the KM line, as we have seen from the RBM el-ph matrix elements for SI and SII tubes shown in Figs. 6–9. In Table I $|D|$ is the averaged value for the two points on the ΓK and KM lines, i.e., $|D| = (|D|_{\Gamma K} + |D|_{KM})/2$. The matrix element $|D|$ have similar values for emission and absorption processes. In Table I we only show $|D|$ for emission processes.

We calculate the relaxation time by the Fermi Golden rule,[16,18]

$$1/\tau = \frac{2\pi}{\hbar}\bar{n}|M|\rho, \tag{25}$$

where ρ is the density of states for the final states. For back scattering,

$$\rho = NS/\pi d_t \hbar v_F, \tag{26}$$

with S the area of a 2D graphite unit cell[16,18] and v_F the electron velocity near the Fermi level.

Table I indicates that for acoustic phonon modes, the el-ph coupling for back scattering mainly comes from the TW mode, which is consistent in the result by Ref. 7. The resulting mean free path can be longer than 1 μm, which agrees with the transport measurements on SWNTs with low bias voltage.[2,3]

For the TW mode, with $q \to 0$, both the matrix element D and the phonon energy $\hbar\omega_{\mathrm{TW}}$ tend to be linear functions of q, i.e., $D = \eta q$ and $\hbar\omega_{\mathrm{TW}} = c_{\mathrm{TW}} q$. The phonon number can be approximated by[7]

$$n + 1 \approx n \approx kT/\hbar\omega_{\mathrm{TW}}. \tag{27}$$

Substituting Eqs. (26) and (27) into Eq. (25), we obtain an expression for the relaxation time of the TW mode,

$$1/\tau = 4S\eta kT/m v_F c_{\mathrm{TW}}^2 d_t. \tag{28}$$

Here η is a constant ($\approx$2.462) describing the el-ph coupling ($|D| = \eta q$) for the TW mode. The mean free path can be obtained from τ by $l = v_F \tau$. By neglecting the weak diameter dependence of η and c_{TW}, we get a simple expression for the scattering length for metallic tubes in the low bias range,

$$\ell_{\mathrm{TW}} = 400.46 \times 10^3 d_t/T, \tag{29}$$

where ℓ_{TW} is in units of nm. A similar expression is given in Ref. 7 with an approximated coefficient 565.49×10^3 larger than 400.46×10^3 shown here.

For high energy phonon modes, the el-ph coupling of back scattering is dominated by the LO, A_1' and one of the E_1' modes. The resulting mean free path for a (10,10) tube is about 76.6 nm, which agrees with that reported by other calculations.[2,6,10,11] The values of the el-ph matrix elements $|D|$ for the LO and A_1' modes are about 6.66 eV/Å and 9.94 eV/Å, respectively, which agrees well with those obtained by recent *ab initio* calculations, which give 6.75 eV/Å and 9.58 eV/Å.[10,47] Moreover, we find that one of the E_1' modes can have a large backscattering el-ph coupling, which has not been reported before. This el-ph coupling comes from the on-site deformation potential.

For high energy phonon modes, the phonon number at thermal equilibrium for absorption and emission processes is approximately zero and 1, respectively. Thus, the relaxation time and mean free path are independent of the temperature. The relaxation time for optical phonon modes at thermal equilibrium is given by

$$1/\tau = \frac{2\pi}{\hbar}|M|\rho, \tag{30}$$

and for back scattering ρ is expressed by Eq. (26). By neglecting the weak diameter dependence of the el-ph matrix elements $|D|$ for the high-energy phonon modes, we get an expression for the scattering length for metallic tubes in the high bias range,

$$\ell_{op} = 56.4 d_t, \tag{31}$$

where ℓ_{op} is in units of nm. A similar expression is given in Ref. 10 but with a coefficient 65 larger than 56.4 shown here. The transport measurements on metallic tubes with high bias voltage show a smaller value (18–20 nm) than that given in Eq. (31).[2,6] It was argued that during high-bias electron transport, the phonons are not in thermal equilbrium and a nonequilibrium phonon occupation is formed, i.e., the phonon number is $\bar{n} > 1$, and this large value reduces the mean free path.[10]

Among the 12 modes, the LO, A_1' and E_1' modes have the largest el-ph coupling. The el-ph coupling for the LO and A_1' mode comes from the off-site deformation potential, while that for the E_1' modes comes from the on-site deformation potential. As we have mentioned, K point phonons are responsible for the Raman G' peaks. The G' feature observed around 2700 cm^{-1} in graphite and SWNT is well known. The G' feature has two peaks for 3D graphite, but both are around 2700 cm^{-1}. The A_1' mode, which has the highest frequency among the six K phonon modes is expected to contribute to the Raman peak around 2700 cm^{-1}. Around the G'-band region of graphite and carbon nanotubes, in addition to the prominent band around 2700 cm^{-1}, a weak band around 2450 cm^{-1} has also been found.[37,38] This band was assigned as a combination of two modes in Ref. 38. However, in Ref. 37, it was argued that the weak band comes from the same branch responsible for the G' phonon around K. In both assignments, at least one E_1' mode around K point is involved. Thus, the on-site deformation potential, which introduces nonzero el-ph coupling for E_1' modes, should be important in explaining the experimentally observed 2450 cm^{-1} Raman peak.

VII. DISCUSSIONS AND SUMMARY

In the present paper, we have developed the el-ph matrix element by considering s, σ, and π orbitals. We find that the

σ orbital mainly affects the el-ph coupling for the RBM and the out-of-plane TO mode, where the vibrations are perpendicular to the tube surface and the curvature effect becomes important. For other phonon modes, the el-ph matrix element based on the Hamiltonian considering only the π orbital provides a good approximation for the el-ph coupling. For this case, the el-ph coupling Eq. (22) is dramatically simplified,

$$D^{\nu}_{a,\mathbf{k}\to a',\mathbf{k}'} = \Bigg(\sum_{s'} C^{*}_{s'}(a',\mathbf{k}') C_{s'}(a,\mathbf{k}) \times \sum_{u,s} \lambda(|\mathbf{R}_{u,s} - \mathbf{r}_{s'}|) \mathbf{e}^{\nu}_{\mathbf{k}'-\mathbf{k}}(\mathbf{R}_{u,s}) \times \sum_{s',s} C^{*}_{s'}(a',\mathbf{k}') C_{s}(a,\mathbf{k}) + \sum_{u} \alpha(|\mathbf{R}_{u,s} - \mathbf{r}_{s'}|) \times \{ \mathbf{e}^{\nu}_{\mathbf{k}'-\mathbf{k}}(\mathbf{R}_{u,s}) e^{-i(\mathbf{k}'-\mathbf{k})\cdot\mathbf{r}_{s'}} - \mathbf{e}^{\nu}_{\mathbf{k}'-\mathbf{k}}(s') \} \Bigg) \cdot \frac{\mathbf{R}_{u,s} - \mathbf{r}_{s'}}{|\mathbf{R}_{u,s} - \mathbf{r}_{s'}|}, \tag{32}$$

where λ and α are the matrix elements for $(\pi\pi)$, and $\mathbf{R}_{u,s} \neq \mathbf{r}_{s'}$.

The RBM is a special mode in SWNTs with regard to the curvature effect. The electronic wavefunction of the π band has a dominant component for the π orbital and has only a small component for the σ orbital. However, as we have mentioned above, $\vec{\alpha}_{\pi\pi}$ and $\vec{\lambda}_{\pi\pi}$ are both along the bond direction and thus they have only a small component perpendicular to the tube sidewall. $\vec{\alpha}_{\pi\sigma}$, on the other hand, is perpendicular to the bond direction and $|\alpha_{\pi\sigma}|$ has a larger value than $\alpha_{\pi\pi}$ (or $|\lambda_{\pi\pi}|$) at $r=1.42$ Å. Thus, $\vec{\alpha}_{\pi\sigma}$ can have a large component perpendicular to the tube surface. The contribution to the el-ph matrix element $g_{o\to o'}$ of the RBM from the σ orbital by the deformation potential $\alpha_{\pi\sigma}$ is then expected to be sufficiently large. However, it is interesting to find that the contribution to $g_{p_z\to p_z}$ from $\alpha_{\pi\sigma}$ is canceled to some extent by the contribution to $g_{p_x\to p_z}$ $(g_{p_z\to p_x})$ and $g_{p_y\to p_z}$ $(g_{p_z\to p_y})$ from $\alpha_{\pi\sigma}$. Fig. 14 shows $|g|$ as a function of θ by considering only the π orbital. Comparing Fig. 14 with Fig. 7, it is seen that π orbital model can approximately describe the family patterns in RBM. The reason is that the curvature effect is partial canceled by the two different contributions mentioned above. However, the σ orbital effect can also be seen. For example, the σ orbital enhances the $|g|$ value for both SI and SII tubes and it also modifies the family patterns, especially for SII tubes.

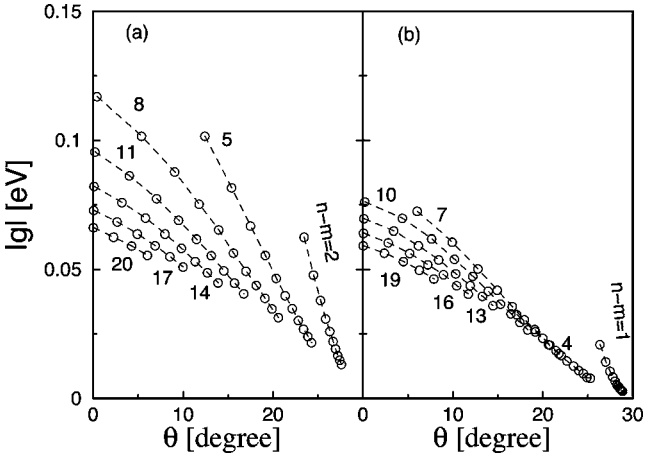

FIG. 14. The el-ph matrix element for the E^{S}_{22} transition for the RBM by considering only the π orbital for (a) SI and (b) SII tubes. The family numbers for $n-m$ are shown in the figures.

In summary, we have calculated the el-ph coupling for SWNTs in the framework of the ETB. The el-ph matrix elements for the RBM and G band modes show nice family patterns. The backscattering mean free path obtained for armchair tubes agrees with the transport measurements on metallic tubes in the low and high bias voltage ranges and is also consistent with other theoretical calculations.[7] In particular, we find that the on-site deformation potential, which is usually not considered in the literature for optical phonons, gives rise to a large el-ph coupling for two E'_1 modes, with one mode for forward scattering and another mode for backscattering. It follows that the on-site deformation potential is important in describing both the transport properties of SWNTs and the G' Raman spectra in carbon.

ACKNOWLEDGMENTS

One of the authors (J.J.) acknowledges Professor Th. Frauenheim and Dr. Th. Köhler for their stimulating discussions and for their unpublished basis functions and Kohn-Sham potential of carbon. One of the authors (R.S.) acknowledges a Grant-in-Aid (No. 16076201) from the Ministry of Education, Japan. Two of the authors (J.J. and R.S.) thank Dr. S. Roche for valuable discussions on transport. MIT authors acknowledge support under NSF Grant No. DMR 04-05538, and the Dupont-MIT Alliance. One of the authors (A.J.) acknowledges financial support from FAPEMIG and PRPq-UFMG, Brazil.

[1] R. Saito, G. Dresselhaus, and M. S. Dresselhaus, *Physical Properties of Carbon Nanotubes* (Imperial College Press, London, 1998).
[2] Ji-Yong Park *et al.*, Nano Lett. **4**, 517 (2004).
[3] A. Bachtold, M. S. Fuhrer, S. Plyasunov, M. Forero, Erik H. Anderson, A. Zettl, and Paul L. McEuen, Phys. Rev. Lett. **84**, 6082 (2000).
[4] Ph. Avouris, MRS Bull. **29**, 403 (2004).
[5] A. Javey *et al.*, Nature (London) **424**, 654 (2003).
[6] A. Javey, J. Guo, M. Paulsson, Q. Wang, D. Mann, M. Lundstrom, and H. Dai, Phys. Rev. Lett. **92**, 106804 (2004).
[7] H. Suzuura and T. Ando, Phys. Rev. B **65**, 235412 (2002).
[8] R. A. Jishi, R. M. Mirie, M. S. Dresselhaus, G. Dresselhaus, and P. C. Eklund, Phys. Rev. B **48**, 5634 (1993).

[9] Z. Yao, C. L. Kane, and C. Dekker, Phys. Rev. Lett. **84**, 2941 (2000).
[10] M. Lazzeri, S. Piscanec, M. Francesco, A. C. Ferrari, and J. Robertson, cond-mat/0503278 (unpublished).
[11] S. Roche, J. Jiang, F. Triozon, and R. Saito, Phys. Rev. Lett. **95**, 076803 (2005).
[12] S. Roche, J. Jiang, F. Troizon, and R. Saito, Phys. Rev. B **72**, 113410 (2005).
[13] J. S. Lauret, C. Voisin, G. Cassabois, C. Delalande, Ph. Roussignol, O. Jost, and L. Capes, Phys. Rev. Lett. **90**, 057404 (2003).
[14] K. Seibert, G. C. Cho, W. Kütt, H. Kurz, D. H. Reitze, J. I. Dadap, H. Ahn, M. C. Downer, and A. M. Malvezzi, Phys. Rev. B **42**, 2842 (1990).
[15] C. Manzoni, A. Gambetta, E. Menna, M. Meneghetti, G. Lanzani, and G. Cerullo, Phys. Rev. Lett. **94**, 207401 (2005).
[16] J. Jiang, R. Saito, A. Grüneis, G. Dresselhaus, and M. S. Dresselhaus, Chem. Phys. Lett. **392**, 383 (2004).
[17] S. M. Bachilo, M. S. Strano, C. Kittrell, R. H. Hauge, R. E. Smalley, and R. B. Weisman, Science **298**, 2361 (2002).
[18] J. Jiang, R. Saito, A. Grüneis, S. G. Chou, Ge. G. Samsonidze, A. Jorio, G. Dresselhaus, and M. S. Dresselhaus, Phys. Rev. B **71**, 045417 (2005).
[19] S. G. Chou, F. P. Filho, J. Jiang, R. Saito, D. Nezich, H. B. Ribeiro, A. Jorio, M. A. Pimenta, Ge. G. Samsonidze, A. P. Santos, M. Zheng, G. B. Onoa, E. D. Semke, G. Dresselhaus, and M. S. Dresselhaus, Phys. Rev. Lett. **94**, 127402 (2005).
[20] Y. Miyauchi, S. Chiashi, Y. Murakami, Y. Hayashida, and S. Maruyama, Chem. Phys. Lett. **387**, 198 (2004).
[21] Y. Oyama, R. Saito, K. Sato, J. Jiang, Ge. G. Samsonidze, A. Gruneis, Y. Miyauchi, S. Maruyama, A. Jorio, G. Dresselhaus, and M. S. Dresselhaus, Carbon (to be published).
[22] S. Reich, C. Thomsen, and J. Robertson, Phys. Rev. Lett. **95**, 077402 (2005).
[23] A. M. Rao, E. Richter, S. Bandow, B. Chase, P. C. Eklund, K. A. Williams, S. Fang, K. R. Subbaswamy, M. Menon, A. Thes, R. E. Smalley, G. Dresselhaus, and M. S. Dresselhaus, Science **275**, 187 (1997).
[24] M. S. Dresselhaus, G. Dresselhaus, R. Saito, and A. Jorio, Phys. Rep. **409**, 47 (2005).
[25] R. M. Martin and L. M. Falicov, in *Light-Scattering in Solids*, edited by M. Cardona (Springer-Verlag, Berlin, 1975), p. 80.
[26] J. Jiang, R. Saito, A. Grüneis, S. G. Chou, Ge. G. Samsonidze, A. Jorio, G. Dresselhaus, and M. S. Dresselhaus, Phys. Rev. B **71**, 205420 (2005).
[27] S. K. Doorn, D. A. Heller, P. W. Barone, M. L. Usrey, and M. S. Strano, Appl. Phys. A: Mater. Sci. Process. **78**, 1147 (2004).
[28] A. Jorio, C. Fantini, M. A. Pimenta, R. B. Capaz, Ge. G. Samsonidze, G. Dresselhaus, M. S. Dresselhaus, J. Jiang, N. Kobayashi, A. Grüneis, and R. Saito, Phys. Rev. B **71**, 075401 (2005).
[29] M. Machón, S. Reich, H. Telg, J. Maultzsch, P. Ordejón, and C. Thomsen, Phys. Rev. B **71**, 035416 (2005).
[30] A. Grüneis, Ph.D. thesis, Tohoku University, Sendai, Japan, 2004.
[31] Ge. G. Samsonidze, R. Saito, N. Kobayashi, A. Grüneis, J. Jiang, A. Jorio, S. G. Chou, G. Dresselhaus, and M. S. Dresselhaus, Appl. Phys. Lett. **85**, 5703 (2004).
[32] V. N. Popov, New J. Phys. **6**, 17 (2004).
[33] D. Porezag, Th. Frauenheim, Th. Köhler, G. Seifert, and R. Kaschner, Phys. Rev. B **51**, 12947 (1995).
[34] F. S. Khan and P. B. Allen, Phys. Rev. B **29**, 3341 (1984).
[35] V. N. Popov, L. Henrard, and P. Lambin, Nano Lett. **4**, 1795 (2004).
[36] V. N. Popov, Luc Henrard, and Philippe Lambin, Phys. Rev. B **72**, 035436 (2005).
[37] T. Shimada, T. Sugai, C. Fantini, M. Souza, L. G. Cançado, A. Jorio, M. A. Pimenta, R. Saito, A. Grüneis, G. Dresselhaus, M. S. Dresselhaus, Y. Ohno, T. Mizutani, and H. Shinohara, Carbon **43**, 1049 (2005).
[38] P. H. Tan, C. Y. Hu, J. Dong, W. Shen, and B. Zhang, Phys. Rev. B **64**, 214301 (2001).
[39] R. Saito and H. Kamimura, J. Phys. Soc. Jpn. **52**, 407 (1983).
[40] C. Fantini, A. Jorio, M. Souza, M. S. Strano, M. S. Dresselhaus, and M. A. Pimenta, Phys. Rev. Lett. **93**, 147406 (2004).
[41] R. Saito, G. Dresselhaus, and M. S. Dresselhaus, Phys. Rev. B **61**, 2981 (2000).
[42] A. Jorio, A. P. Santos, H. B. Ribeiro, C. Fantini, M. Souza, J. P. M. Vieira, C. A. Furtado, J. Jiang, R. Saito, L. Balzano, D. E. Resasco, and M. A. Pimenta, Phys. Rev. B **72**, 075207 (2005).
[43] A. Jorio, D. A. Heller, M. S. Strano, C. Fantini, Y. Oyama, J. Jiang, R. Saito, M. S. Dresselhaus, and M. A. Pimenta, Appl. Phys. Lett. (to be published).
[44] L. Wirtz and A. Rubio, Solid State Commun. **131**, 141 (2004).
[45] J. Maultzsch, S. Reich, C. Thomsen, H. Requardt, and P. Ordejon, Phys. Rev. Lett. **92**, 075501 (2004).
[46] Ge. G. Samsonidze, R. Saito, A. Jorio, M. A. Pimenta, A. G. Souza Filho, A. Grüneis, G. Dresselhaus, and M. S. Dresselhaus, J. Nanosci. Nanotechnol. **3**, 431 (2003).
[47] S. Piscanec, M. Lazzeri, F. Mauri, A. C. Ferrari, and J. Robertson, Phys. Rev. Lett. **93**, 185503 (2004).